Journal of Power Sources 196 (2011) 5564–5572

Contents lists available at ScienceDirect

Journal of Power Sources

journal homepage: www.elsevier.com/locate/jpowsour

Simulated start–stop as a rapid aging tool for polymer electrolyte fuel cell electrodes

Christoph Hartnig [1], Thomas J. Schmidt [*,2]

BASF Fuel Cell GmbH, Industrial Park Hoechst, D-65926 Frankfurt am Main, Germany

ARTICLE INFO

Article history:
Received 1 November 2010
Received in revised form
30 December 2010
Accepted 16 January 2011
Available online 26 January 2011

Keywords:
High temperature PEFC
Polybenzimidazole (pbi)
Rapid aging
Accelerated aging
Fuel cell diagnostics

ABSTRACT

The corrosion stability of supported catalysts as employed in state of the art intermediate temperature polymer electrolyte fuel cells has been studied by means of simulated start–stop cycling (150 cycles). The carbon dioxide formation from the air electrode has been monitored during repeated cycling runs and the loss of catalyst support has been correlated with performance drops. Degradation effects have been studied at different current densities in order to differentiate between kinetic and mass transport effects. Finally, correlations of this accelerated aging tool with a more realistic durability test over 4000 h and 157 start–stop cycles have been made and the good agreement between simulated and realistic approaches has been confirmed, demonstrating the high value of the experimental approach and analysis.

1. Introduction

The commercialization of hydrogen fuel cells is a key issue for enabling a sustainable hydrogen-based economy. Low and intermediate temperature polymer electrolyte fuel cells (PEFCs) are a promising and far-developed technology for automotive, stationary and small portable applications. Although lots of component development and system field testing have been performed over the years, durability of stack and stack components, such as membrane electrode assemblies (MEAs), membranes, electrodes, gaskets or bipolar plates is still a major concern [1,2]. In order to be commercially successful, e.g., in the residential sector, the lifetime requirements for residential applications of more than 40,000 h have to be reached to ensure a viable alternative to state of the art power supplies. Polybenzimidazole (PBI)-based intermediate-temperature membrane electrode assemblies (MEAs) are a viable way for combined heat and power (CHP) applications as they are operated at temperatures between 120 °C and 180 °C making them especially suitable for operation with reformed-hydrogen-based feed gases [3–5]. Due to these high operating temperatures, CO tolerances up to 3% can be achieved [6,7]. Additional fuel gas impurities [8] (inorganic or organic, such as H_2S or methanol) can be tolerated to a much higher concentration compared to low temperature fuel cells based on PFSA type [9,10] or hydrocarbon membranes [11,12]. As a consequence, the gas purification can be simplified in a fuel cell system using a fuel processor for reforming hydrocarbon-based fuels and additional gas purification such as shift-reaction zones or preferential CO oxidation stages can be avoided.

One of the challenges in the development of membrane electrode assemblies is the impossibility to perform significant numbers of durability tests in the laboratory on component basis for the required lifetimes mainly due to time and test station constraints. Since tests for several thousands of hours in order to find out if a component advancement can last that long are virtually impossible, rapid or accelerated aging tests are necessary which study specific degradation modes in short time periods and being able to correlate these results with findings from realistic lifetime tests. For proper correlations between accelerating and realistic conditions, the degradation mode to be studied needs to be mechanistically well understood.

Drivers for the development of accelerated aging tests including predictions of lifetime is typically the fuel cell industries. Early applications can be found in the development of phosphoric acid fuel cells (PAFC), see e.g., Ref. [13] where a perturbation testing technique has been applied to study main effects on PAFC cell degradation. Over the last years, statistical methods were engaged, e.g., design of experiments (DoE) [14] and Taguchi quality engineering methods [15] especially for component durability

* Corresponding author. Tel.: +41 56 310 5765.
E-mail address: thomasjustus.schmidt@psi.ch (T.J. Schmidt).
[1] Present address: Chemetall GmbH, Frankfurt, Germany.
[2] Present address: Paul Scherrer Institute, Electrochemistry Laboratory, Villigen PSI, Switzerland.

0378-7753/$ – see front matter © 2011 Elsevier B.V. All rights reserved.
doi:10.1016/j.jpowsour.2011.01.044

studies. A recent chapter by Hicks and Pierpoint summarizes some approaches for accelerated lifetime testing and statistical lifetime modeling [16]. As these authors point out, lifetime can never be assumed to be a single data point, but must be assumed to be a statistical distribution. For these reasons, significant amounts of data need to be acquired and the correct lifetime model needs to be applied. In reality, however, especially when it comes to full cell or stack testing it is very difficult to have enough data which can be fitted by the correct model and predictions at some point need to be checked by lifetime tests in order to avoid misleading predictions.

In this paper we make an attempt to correlate results from rapid aging tests to results from a realistic durability test. In more detail, we demonstrate how simulated start–stop (SSS) operation of a single intermediate temperature fuel cell can be used to study cathode stability and allows for the lifetime prediction of the MEA under realistic fuel cell operation conditions. Three different cathode materials have been studied under simulated start–stop conditions, *i.e.*, we purposely passed an alternating hydrogen/air (air/hydrogen) front through the fuel electrode compartment of a single fuel cell and measured the air electrode carbon corrosion product *viz.*, CO_2. In parallel to CO_2 quantification, the cathode performance degradation was monitored electrochemically and the different cathode loss terms (ohmic, kinetic, and mass transport) are separated from these data. After the SSS test, post-mortem electron microscopy helped to image the cathode catalyst degradation.

2. Electrode degradation during start/stop operation

Before a more detailed description of the performed work is given, we shortly review the effects of fuel cell start–stop/shutdown on the cathode. During start/stop cycling the two predominant mechanisms which can affect MEA durability is (i) corrosion of the cathode due to potential excursions to $E > 1.3$ V [17–19] and (ii) electrolyte redistribution due to volume expansions/contractions. The latter mode is unique to fuel cell operation with at least partly liquid electrolytes whereas the first is a more general mode observed also in low temperature PEFCs [20–22]. Cathode carbon corrosion during start stop cycling occurs when the cathode electrolyte potential excurses to high values when H_2/air (air/H_2) fronts are passing through the anode while the cathode compartment is filled with air (see e.g. Fig. 4 in Ref. [17]). Since the anode potential is basically defined by the hydrogen potential, the present oxygen in the anode (fuel electrode) will be instantaneously reduced to water. During the oxygen reduction reaction, ORR, at the anode side (fuel electrode), the used protons are generated in an oxidation reaction at the opposite side at the cathode with either one of the following reactions: carbon oxidation (Eq. (1a)), oxygen evolution (Eq. (1b), faradaic reactions) and/or oxidation of Pt (Eqs. (1c) and (1d), pseudo-capacitive reactions).

$$C + 2H_2O \rightarrow CO_2 + 4H^+ + 4e^- \quad E^0 = 0.206\,V [23] \tag{1a}$$

$$H_2O \rightarrow 1/2O_2 + 2H^+ + 2e^- \quad E^0 = 1.229\,V \tag{1b}$$

$$Pt + H_2O \rightarrow PtOH + H^+ + e^- \tag{1c}$$

$$PtOH \rightarrow PtO + H^+ + e^- \tag{1d}$$

The equilibrium potentials of reaction (1c) and (1d) have been estimated to be 0.85 V and 1.0 ± 0.05 V vs. the reversible hydrogen electrode. [24] In parallel to the proton forming reactions, (1a)–(1d), Pt can be dissolved according to Eq. (1e):

$$Pt \rightarrow Pt^{2+} + 2e^- \tag{1e}$$

By examination of the respective Pourbaix diagram [25,26] reaction (1e) is expected to occur in a triangular region under the present pH conditions between approximately 0.95 V and 1.25 V. By following the nomenclature of Reiser et al. the region where one or more of these oxidation reactions occur on the cathode (air electrode) is the so-called reverse current region [19]. Simultaneously, in the normal operation region hydrogen and oxygen is oxidized and reduced, respectively, as usual. Both regions are electrically connected through the GDL materials. Basically, the fuel cell is internally short circuited. One can consider the normal operation region as a power source and the reverse current region as a power sink. Locally, around the H_2/air (air/H_2) front the potential of the cathode in the intermediate-temperature MEA can be as high as 1.3 V as we have been measuring using the dual cell setup [17]. Precautions to avoid carbon corrosion and/or occurrence of reactions (1a)–(1e) under such conditions as well as detailed description of similar mechanisms are well summarized in publications by Perry et al. [27,28].

3. Experimental

3.1. Materials

All measurements have been performed using 50 cm^2 intermediate-temperature MEAs with a PBI/phosphoric acid based membrane as described in Refs. [29,30]. The anode contains a Vulcan XC 72 supported Pt catalyst with 1 $mg_{Pt}\,cm^{-2}$. For the cathodes, three different catalyst materials have been employed using 30% Pt/Vulcan XC72 (1 $mg_{Pt}\,cm^{-2}$ and 2.33 $mg_C\,cm^{-2}$, sample A), 30% Pt-alloy/Vulcan XC72 (0.75 $mg_{Pt}\,cm^{-2}$ and 2.33 $mg_C\,cm^{-2}$, sample B) and 20% Pt-alloy/SC (stabilized carbon, 0.75 $mg_{Pt}\,cm^{-2}$ and 4.0 $mg_C\,cm^{-2}$, sample C). All three different catalysts have rather similar crystallite sizes of 3.5–4 nm. All MEAs were manufactured at BASF Fuel Cell GmbH, Frankfurt, Germany.

3.2. Electrochemical measurements and simulated start–stop cycles

All measurements were carried out in 50 cm^2 single cells using surface sealed graphite flow field plates. MEA break in was done for 15 h at 160 °C and 0.2 A cm^{-2} under hydrogen/air (stoichiometries 1.2/2) and ambient pressure. After break-in, the temperature has been increased to 180 °C and initial *I*–*E*-curves have been recorded to determine beginning of life (BOL) performance using H_2/air (stoichiometry 1.2/2) and H_2/O_2 (stoichiometry 1.2/9.5). During all electrochemical measurements, the fuel cell impedance was recorded using 2 kHz AC-impedance measurements. After the initial BOL *I*–*E*-curves, 150 simulated start–stop cycles have been performed according to the following protocol (denotation of the electrodes follows the proposal in Ref. [28]): the fuel electrode and air electrode gas flows were kept constant at 3.3 NL h^{-1} and 20 NL h^{-1}, respectively. The air electrode gas was air in all cases, whereas the fuel electrode gas was switched in 90 s intervals between pure hydrogen and air by means of an automated valve allowing for H_2/air (air/H_2 resp.) fronts passing through the fuel electrode flow field. No external load was applied during the gas cycles (open circuit conditions). After every 50 full cycles (*i.e.*, one complete switching from hydrogen to air and vice versa), a set of H_2–air and H_2–O_2 polarization curves was recorded. End of life (EOL) was defined after 150 simulated start–stop cycles. During the SSS cycles, the CO_2 content of the cathode exhaust gas was monitored online by means of a CO_2 NDIR-sensor (Sick Sidor Maihak Unor 6N) with measurement intervals of 2 s.

In parallel, we operated one MEA with a sample C cathode (20% Pt-alloy/SC, 0.75 $mg_{Pt}\,cm^{-2}$) for 4000 h (H_2–air, stoichiometry 1.2/2, $T = 180$ °C, ambient pressure) and a total of 157 start–stop cycles. The start/stop cycling of this MEA is performed in a way that the cell was continuously operated for 16 h at 0.2 A cm^{-2} before cell operation has been stopped and the cell was allowed to cool down

to 25–30 °C for 8 h. Note that the cell was not actively purged with any gas during the stop period and no other gases were flowing during the stop phase. After the 8 h stop period, the cell has been restarted again, *i.e.*, one shut down per day is performed. For the startup, the cell was heated to 80 °C before the hydrogen flow of 3 NL h^{-1} and the air flow of 5 NL h^{-1} were started. At 140 °C, the cell was switched to 0.2 A cm^{-2}. The gas outlets of the cell are kept open throughout the whole experiment directly at the cell end plates. That is under all conditions, approximately two centimeters from the cell outlets in upstream direction the flow field channels begin. That way, a short diffusion path is given which allows easy equilibrium of the gases in the cell with ambient air and it is ensured that air can diffuse in the anode compartment resulting in a diffusive H_2/air front. The residence time of this front, however, is undefined. In this durability test we determined hydrogen cross-over at BOL and EOL electrochemically according to the method described in Ref. [31]. At beginning of life, hydrogen cross-over is equivalent to less than 1 mA cm^{-2}, at end of life of this particular test cross-over amounts to 28 mA cm^{-2}.

3.3. SEM imaging

In order to directly visualize MEA degradation, we performed post-mortem imaging using a scanning electron microscope (Zeiss Leo1430) equipped with an energy dispersive X-ray analyzer (Oxford Instruments). EDX analysis is performed only for a qualitative distinction of the employed materials. Several scalpel-cut cross sections of the used MEAs have been imaged. All images shown were taken in backscattering mode, *i.e.*, visual sensitivity to heavy elements is given and brighter areas indicate an increased content of heavy elements compared to darker ones.

3.4. Determination of individual overpotentials

In order to determine individual cathode loss contributions, we used the data from the H_2–air and H_2–O_2 *I*–*E* curves. The calculation of the individual overpotentials, *i.e.*, kinetic overpotentials for the ORR, η_{ORR}, and cathodic mass transport overpotentials, η_{mtx}, was achieved using a Tafel slope analysis with a procedure described in detail in Refs. [17,32,33]. In short, the cell potential corrected for Ohmic contribution can be given by Eq. (2):

$$E_{\text{cell,IR-free}} = E^0(p_{H_2/O_2/H_2O}, T) - \eta_{ORR} - \eta_{\text{cathode,mtx}} - \eta_{HOR} - \eta_{\text{anode,mtx}} \quad (2)$$

where $E^0(p_x,T)$ represents the temperature and partial pressure dependent (H_2, O_2, and H_2O) equilibrium potential, η_{ORR} and η_{HOR} the kinetic overpotentials for the oxygen reduction and hydrogen oxidation reaction and $\eta_{x,mtx}$ the mass transport overpotentials on the cathode and anode, respectively. The temperature and partial pressures dependent equilibrium potential $E^0(p_x,T)$ is calculated according to Eq. (3):

$$E^0(p_{H_2/O_2/H_2O}, T) = E^{0,*} + \frac{\partial E^{0,*}}{\partial T} \cdot (T - 298\,\text{K}) + \left(\frac{2.303RT}{2F}\right) \log\left(\frac{\tilde{p}_{H_2} \cdot \tilde{p}_{O_2}^{0.5}}{\tilde{p}_{H_2O}}\right) \quad (3)$$

where the first term, $E^{0,*}$, is the equilibrium potential at 298 K and 101325 Pa calculated from ΔG values for gas phase water [34]; the second term is used to correct $E^{0,*}$ for the temperature, calculated using ΔS values for gas phase water [34]; the third Nernstian term corrects $E^{0,*}$ for the individual partial pressures. $\tilde{p}_{H_2}$, $\tilde{p}_{O_2}$, $\tilde{p}_{H_2O}$ are the mean partial pressures under operation conditions of hydrogen, oxygen and water, respectively, normalized to 101325 Pa.

Given that consensus is emerging for the fact of negligible anodic polarization and the pure kinetic control of the oxygen polarization curve (*i.e.*, in the applied current range, the Tafel slope for pure oxygen operation is approximately 2.3 RT/F), Eq. (2) reduces to:

$$E_{\text{cell,IR-free}} = E^0(p_{H_2/O_2/H_2O}, T) - \eta_{ORR} \quad (4)$$

By proper calculation of $E^*(p_x,T)$, the oxygen reduction overpotential can be determined by Eq. (4) from the measured oxygen polarization curve which follows an oxygen partial pressure dependent Butler–Volmer expression. The theoretical Tafel line for air polarization should be just shifted to lower cell potentials, by ΔE_{O_2-air} given by:

$$\Delta E_{O_2-air} = \Delta E^0 + b \cdot \gamma \cdot \log\left(\frac{p_{O_2}}{p_{air}}\right) \quad (5)$$

with ΔE^0 being the difference between the equilibrium potentials for pure oxygen and air, b and γ are the Tafel slope (b = 2.3 RT/F) and the kinetic reaction order ($\gamma \approx 0.52$ [35]; defined as the logarithmic change of the current density with the oxygen partial pressure at constant temperature and overpotential) and p_x being the partial pressures for pure oxygen and air. Deviations from the theoretical Tafel line for air polarization to lower cell potentials can be considered to be cathodic mass transport overpotentials. All Tafel slopes in this study were found to be between 90 and 100 mV dec^{-1} in a current density range of up to 0.5 A cm^{-2} closely reflecting the theoretical expected value of 89 mV dec^{-1} at 180 °C (2.3 RT/F). Note that current densities to determine real Tafel slopes were corrected for hydrogen cross-over currents.

The changes in oxygen overpotentials plotted in Fig. 4a and c is calculated by Eq. (6):

$$\Delta\eta_{ORR} = \eta_{ORR,t} - \eta_{ORR,BOL} \quad (6)$$

with $\eta_{ORR,t}$ and $\eta_{ORR,BOL}$ being the overpotential at given operation time and at beginning of life, respectively. The changes in mass transport overpotentials plotted in Fig. 4b and d is calculated by Eq. (7):

$$\Delta\eta_{mtx} = \eta_{mtx,t} - \eta_{mtx,BOL} \quad (7)$$

with $\eta_{mtx,t}$ and $\eta_{mtx,BOL}$ being the overpotential at given operation time and at beginning of life, respectively.

4. Results

4.1. Simulated start–stop cycling

As described in the previous section 150 simulated start–stop cycles were applied to the three different cathodes A, B, and C using 1 mg_{Pt} cm^{-2} 30% Pt/Vulcan XC72, 0.75 mg_{Pt} cm^{-2} 30% Pt-alloy/Vulcan XC72, and 0.75 mg_{Pt}/mg_{Pt} cm^{-2} 20% Pt/SC, respectively. An example of 20 cycles with the concomitant cell voltage changes (MEA with cathode sample C) during the simulated start–stop cycles are shown in Fig. 1a. During the presence of H_2 on the fuel side, the cell potential is the typical open circuit potential of approximately 0.95 V. When the fuel electrode gas is switched to air, the cell potential is dropping to approximately zero. During the purging of the hydrogen with air or vice versa, next to the formed H_2/air (air/H_2) front the local cathode potential is driven to approximately 1.3 V as we have been measured in a previous study using the dual-cell setup [17]. In parallel to the simulated start–stop driven voltage cycle, the CO_2 concentration (reaction (1a)) in the air electrode exhaust was measured (Fig. 1b), following a cyclic pattern with sharp CO_2 concentration rises once the hydrogen or air are replaced by the respective other gas, that is, once the H_2/air (air/H_2) front is passing through the fuel electrode. The residence time for one mixed gas front to pass through the fuel electrode flow field

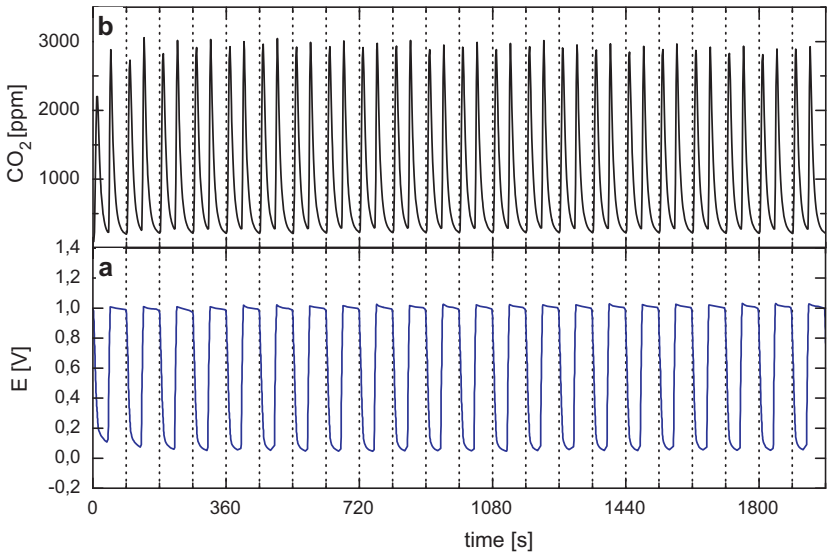

Fig. 1. (a) Cell voltage during periodic simulated start–stop cycles (T = 180 °C, ambient pressure, fuel electrode 3.3 NL h^{-1} H_2 or air; air electrode 20 NL h^{-1} air, sample C cathode). (b) On-line carbon dioxide concentration in air electrode exhaust gas during simulated start–stop cycles.

is approximately three seconds. The tailing of the CO_2 evolution peak until the signal drops back to zero is a result of diffusive processes of CO_2 within both the air electrode gas diffusion layer and its flow field and certainly the total volume of the air electrode/CO_2 sensor total volume. As expected for long residence times as used in this study (3 s), the CO_2 production for the simulated start and simulated stop is identical within ±5%, pointing to the fact that pseudo-capacitive effects only play very minor roles [21]. The CO_2 is considered to be produced from oxidation of the catalyst carbon support in the catalyst layers, although also the gas diffusion layers contain carbon-based materials. Ideally, however, the gas diffusion layer does not contain significant amounts of ionomers/electrolyte and, therefore, is not electrochemically contacted.

4.2. Performance changes during simulated start–stop cycles

Characteristic *I–E*-curves have been recorded employing different gases in order to quantify kinetic and mass transport related loss contributions caused by the carbon support corrosion. As expected, the overall performance of the MEAs using alloy cathode catalysts is approximately 20–25 mV higher than for pure Pt cathodes, indicating the typically found improved alloy cathode kinetics [36–39]. In Fig. 2 a set of curves (sample C cathode) taken during the simulated start–stop cycling is given as an example: in general, a downward shift of the complete curve from BOL to the end of the first 50 cycles has been observed; in the ongoing cycling the performance drops significantly in the mass transport regime with decreasing absolute differences between the individual curves. The polarization curves for sample A and B cathodes, respectively, can be found as supplementary material. For comparison of the IR-corrected voltage changes of the different electrodes, Fig. 3 shows the voltage degradation at 0.3 A cm^{-2} and 0.7 A cm^{-2} in order to get a first impression on the extension of the performance loss. Clearly, at the lower current density the highest degradation is observed from the cathode with the pure Pt/Vulcan catalyst (sample A) and with almost 80 mV voltage loss at EOL, followed by the Pt-alloy/Vulcan catalyst (approximately −65 mV at EOL) and, the Pt-alloy catalyst on stabilized carbon. At the higher current density, 0.7 A cm^{-2}, both cathodes with Vulcan supported catalysts show very similar behavior (∼ −110 mV at EOL), whereas the cathode employing the stabilized carbon support shows the lowest degradation with only −70 mV at EOL. In order to separate between kinetic and mass transport contributions to the overall degradation illustrated in Fig. 3, the Tafel slope analysis as described in detail in Section 3.3 was employed. Using Eq. (6), the relative changes of the oxygen reduction overpotential at 0.1 A cm^{-2} with respect to BOL are calculated (Fig. 4a). Obviously, both alloy catalysts show very similar kinetic degradation behavior with around 35 mV higher overpotentials after 150 cycles as compared to the new MEAs. The MEA using the pure Pt/Vulcan catalyst, however, shows significant bigger changes in ORR kinetics with around 60 mV higher ORR overpotential at EOL. In the mass transport regime at 0.7 A cm^{-2} (Fig. 4b), the superiority of the Pt-alloy catalyst on the stabilized carbon support is evident. The main increase in mass transport overpotentials is observed within the first 50 cycles; afterwards the mass transport overpotentials remain almost constant at around 20 mV. SSS cycling of both cathodes using the Vulcan supported catalysts results in similar changes in mass transport behavior with increases of approximately 60 mV at EOL for the cathodes with 30% Pt/Vulcan and 30% Pt-alloy/Vulcan, respectively.

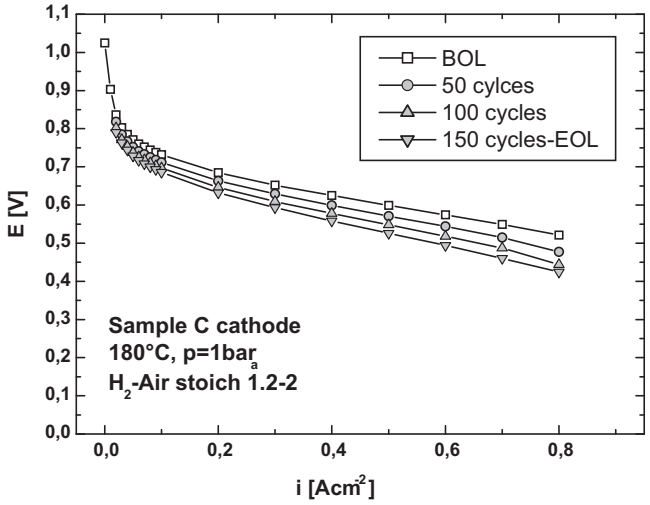

Fig. 2. *I–E*-curves (H_2/air, stoichiometry 1.2/2, 180 °C, ambient pressure) taken at beginning of life, after 50 cycles, 100 cycles and 150 cycles (end of life), respectively (sample C cathode).

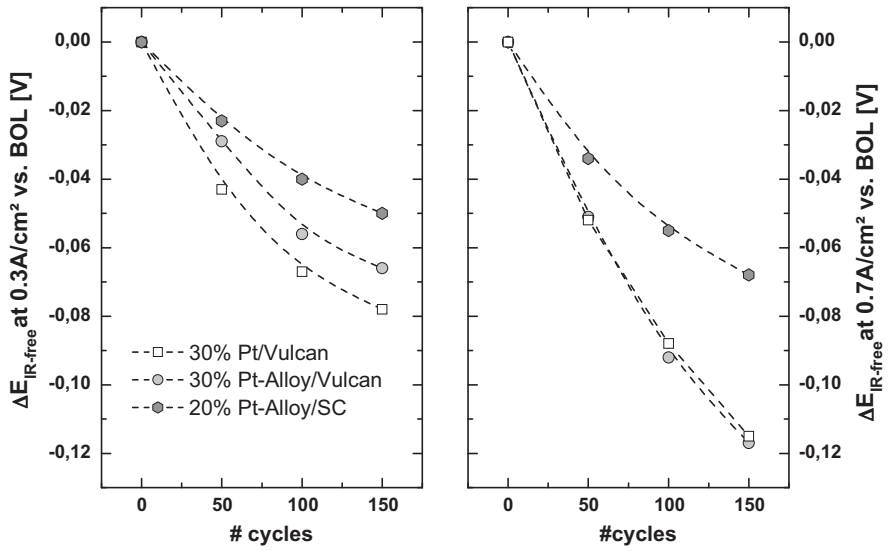

Fig. 3. Relative performance decrease vs. BOL as function of simulated start–stop cycles at 0.3 A cm^{-2} and 0.7 A cm^{-2} deduced from *I–E* curves for cathodes with 30% Pt/Vulcan (sample A), 30% Pt-alloy/Vulcan (sample B) and 20% Pt-alloy/SC (sample C).

In order to find a correlation between the kinetic and mass transport losses as a function of oxidized catalyst carbon support, we carefully analyzed the CO_2 concentration signal from the cathode exhaust (Fig. 1) to determine the molar CO_2 production rate and the total amount of CO_2 produced within each 50 cycles of the SSS test, which also represents the total amount of carbon oxidized in the considered cycles (see Eq. (1a)). Finally, we are able to plot the relative kinetic (Fig. 4c) and mass transport (Fig. 4d) losses as a function of the relative loss of carbon from the catalyst carbon support. Whereas kinetic changes do not appear to be in (direct) relation to the loss of carbon from the catalyst support, mass transport losses are clearly correlated to the amount of oxidized carbon from the catalyst support.

4.3. Performance changes during 4000 h realistic test

In parallel to the simulated start–stop cycles we also performed a realistic durability test in which the test cell was operated for a total of 4000 h including daily start–stops (in total 157 start–stop cycles) according to the protocol described in Section 3.2. Operation of this cell was at 0.2 A cm^{-2} (Fig. 5). Voltage degradation at this current density can be determined to approximately 19 μV h^{-1} or 0.48 mV/cycle. As clearly illustrated in Fig. 5 main degradation

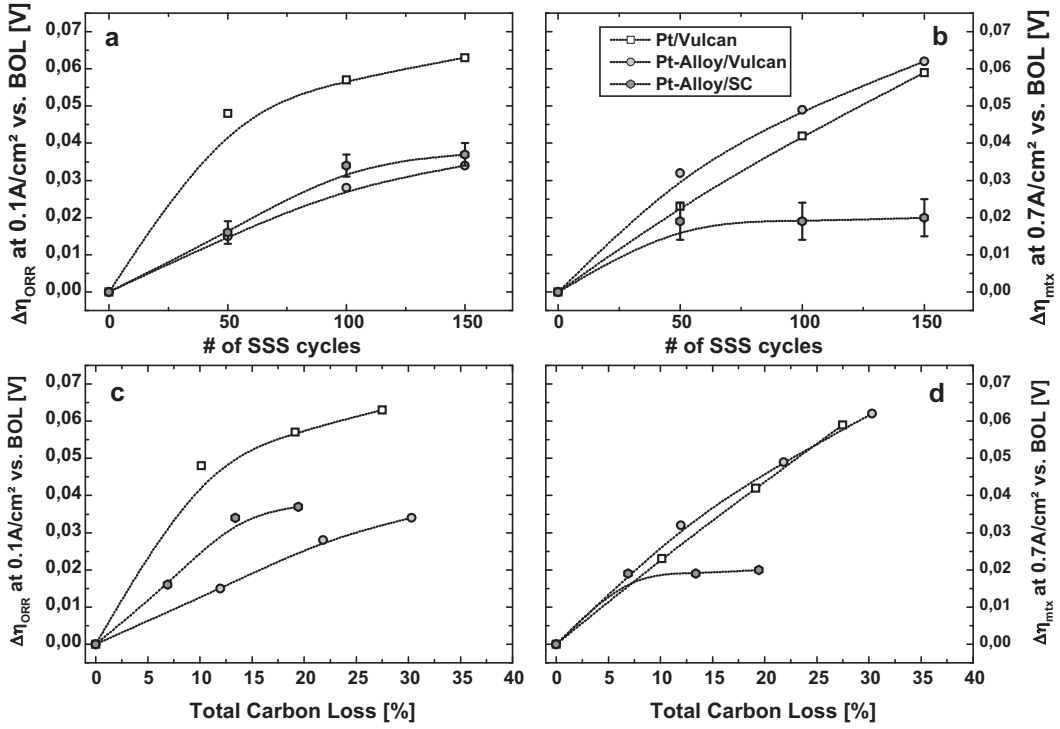

Fig. 4. Increase of ORR (a; at 0.1 A cm^{-2}) and mass transport (b; at 0.7 A cm^{-2}) overpotentials vs. BOL (Eqs. (6) and (7)) as function of number of simulated start/stop cycles. Calculation of individual overpotentials as described in Section 3.3 and correlation of overpotential changes vs. BOL as function of relative amount of oxidized carbon from the catalyst support (c and d) deduced from the online CO_2 production rate during simulated start/stop.

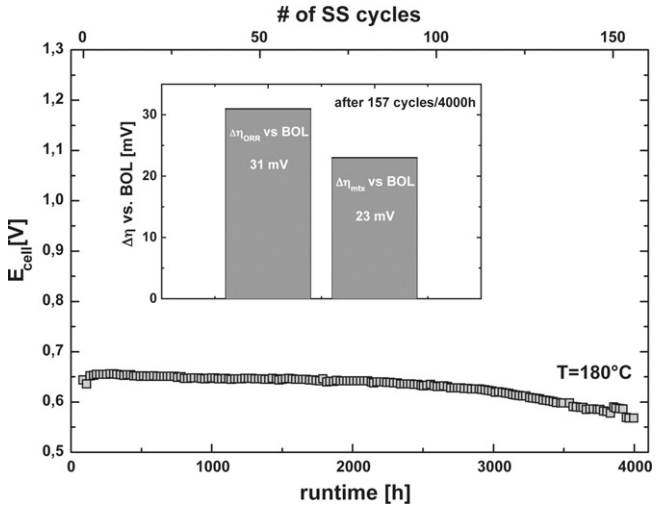

Fig. 5. Realistic durability test of a MEA with sample C cathode (20% Pt-alloy/SC) over 4000 h and 157 start–stop cycles (H_2–air, stoichiometry 1.2/2, T = 180 °C, ambient pressure, open gas outlets). Inset: increase in kinetic ORR (at 0.1 A cm^{-2}) and cathodic mass-transport overpotentials (at 0.7 A cm^{-2}) vs. BOL, respectively, at the end of the 4000 h/157 cycles test (conditions as given above).

starts after the first 2500 h operation time whereas during operation before this point the MEA appears to be very robust. In order to determine the individual overpotentials, we performed and analyzed polarization curves at BOL and EOL. The increase in ORR kinetic and cathodic mass-transport overpotentials from BOL to the end of the test after 4000 h/157 start–stop cycles can be determined to $\Delta\eta_{\mathrm{ORR,0.1\,A\,cm^{-2}}} = 31$ mV and $\Delta\eta_{\mathrm{mtx,0.7\,A\,cm^{-2}}} = 23$ mV (inset of Fig. 5). At the end of the test, the MEA showed a hydrogen crossover equivalent to ~28 mA cm^{-2}. One of the reasons is some edge sealing failure, which will be studied in more detail in the future and is not part of this work.

4.4. Post mortem SEM analyses

For a primary qualitative estimation of the degradation effects, SEM images of cross sections of MEA samples have been taken. The SEM images were recorded in electron backscattering mode, where the intensity is directly proportional to the atomic number of the elements imaged, *i.e.*, heavy elements like Pt can be already easily discriminated from the other light elements in the MEAs (e.g., C, N, P, and F). As a representative example the respective images of the MEA with sample C at BOL (a), after SSS (b) and after realistic cycling (c) are displayed in Fig. 6. On all images shown, the cathode (air electrode) is on the left hand side, followed by the membrane in the center and the anode (fuel electrode) on the right hand side. On all samples, the fuel electrode (right side) appears to be unaffected by the testing conditions, whereas significant differences can be observed after SSS and realistic cycling compared to conditions at BOL on the air electrode. Specifically, most striking is the approximately 5–7 μm thick layer of enriched Pt on the membrane-air electrode interface (Fig. 6b, simulated start–stop cycling) concomitant with a Pt depleted (catalyst) carbon layer. Similarly, the realistically cycled and operated cell (Fig. 6c) shows an approximately 1–2 μm thick enriched Pt layer at the same position. Membrane thickness in Fig. 6c after 4000 h/157 start–stop cycles operation is reduced to approximately 25 μm, whereas the membrane thickness of approximately 45–50 μm at BOL (Fig. 6a) is almost completely retained after SSS cycling (Fig. 6b). In general, the thickness of the air electrode catalyst layer after start–stop cycling is only 85–90% of the original air electrode catalyst layer (both in the SSS test and the realistic test).

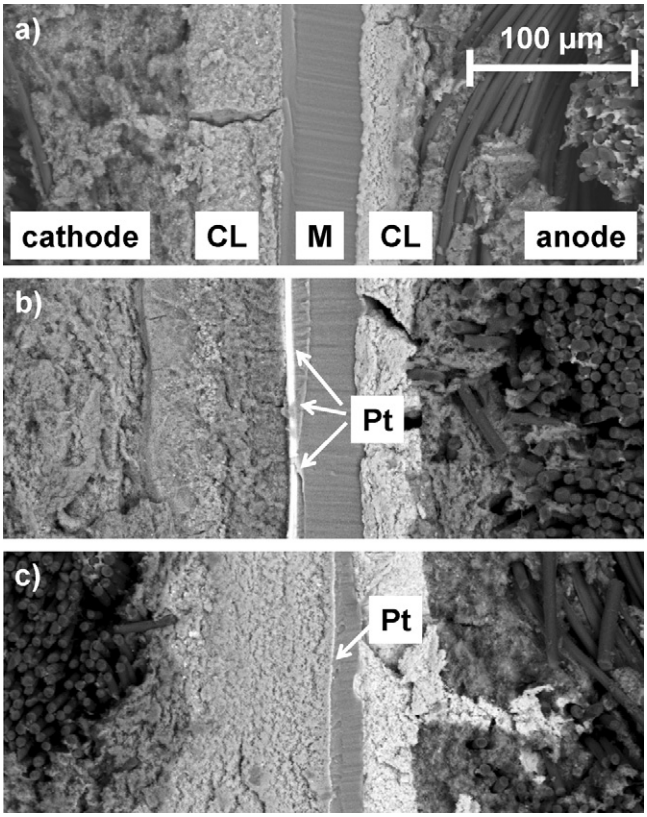

Fig. 6. SEM cross-sections (backscattering mode) of (a) a virgin MEA with sample C cathode (b) MEA with sample C cathode after 150 simulated start/stop cycles and (c) MEA with sample C cathode after 4000 h/157 cycles taken from the realistic durability test (M: membrane, CL: catalyst layer).

The SEM images of the MEAs with cathode sample A and B after SSS cycling in general display very similar features as the sample C cathode in Fig. 6b, *viz.* the formation of the metal layer at the membrane-catalyst layer interface and a Pt depleted catalyst layer. It should be noted that the preparation of sample A and B MEAs with Vulcan XC72 supported catalyst have been more difficult to prepare due to some lost integrity of the respective electrodes after extensive corrosion. For completeness, these SEM images can be found in supplementary data.

5. Discussion

We studied the impact of simulated start–stop cycling on different air electrode (catalyst) materials employing two Vulcan XC72 supported Pt and Pt-alloy catalysts as well as a Pt-alloy catalyst on a stabilized carbon. During SSS cycling which was realized by switching the gas on the air electrode from hydrogen to air and vice versa the CO_2 production from the air electrode is monitored in situ. The major findings on degradation effects resulting from SSS can be summarized as follows: (i) kinetic losses for both alloy electrodes are almost identical and significantly lower than on the pure Pt-catalyst electrode (Fig. 4a); (ii) mass transport losses on the Vulcan XC72 supported catalysts are identical and significantly higher than mass transport losses on the electrodes using the stabilized carbon as catalyst support; (iii) whereas – as expected – no correlation between kinetic losses and relative amounts of oxidized carbon support is found, the increase of mass transport overpotentials is a clear function of amount of oxidized carbon from the catalyst support.

In the following, we will shortly discuss these findings in the light of the underlying processes during start–stop operation of a

fuel cell. Interestingly, effects on the ORR kinetics of the different catalyst clearly demonstrate differences between pure Pt and Pt-alloy catalysts, indicating that through alloying of Pt with a base metal, e.g., Co, Ni, or Fe, the catalyst can be stabilized. That is, the alloy catalysts do show significant less kinetic degradation compared to a pure Pt catalyst. Whereas the kinetic decay for both alloy catalysts is about 35 mV, corresponding to ca. 2.4 times slower kinetics (or, to a reduction of the effective catalyst surface area by this factor), the decay for the pure Pt catalyst is 60 mV or a factor 4.7 slower kinetics (the factors are calculated using the theoretical Tafel slopes of 89 mV dec^{-1} under the applied conditions; the measured Tafel slopes are all between 90 and 100 mV dec^{-1}). Very similar effects have been reported by Ball et al. in their studies on PtCo catalyst stability in low temperature PEFCs. [40] As visualized in the SEM pictures (Fig. 6a vs. b), upon the simulated start–stop cycling induced voltage excursions to approximately 1.3 V on the air electrode, Pt is redistributed to form an enriched layer at the membrane/catalyst layer interface. As a consequence, effective catalyst surface area is lost resulting in reduced ORR kinetics. Although no metal is found in the membrane, it cannot be excluded that some Pt or any metallic catalyst component is transported to the anode in its ionic form (Me^{x+}) and deposited there; this effect has not been studied in more detail here. The effect of Pt layer formation upon air electrode potential cycling is well known and has been reported before in the literature [39,41–43]; it can be described as a combination of several effects [41,44]: (i) catalyst agglomeration triggered by carbon corrosion; (ii) electrochemical Ostwald-ripening; (iii) coalescence of particles via nanocrystallite migration on the support. It cannot be determined from this study which of these effects is playing the predominant role for triggering catalyst kinetic losses and a combination appears to be most realistic. However, the effect of extensive voltage cycling on a low-temperature PEFC cathode using acid treated Pt_3Co/carbon as catalysts was demonstrated in a recent paper by Shen et al. [39] which at least can be qualitatively compared to the results obtained in our simulated start–stop cycling tests. In the study of Shen, the cathode was cycled between 0.65 V and 1.05 V for 24 h (H_2/N_2 setup, 100 mV s^{-1}, resulting in 10800 cycles) at fully humidified 80 °C as compared to our 150 simulated start–stop cycles between approximately 0.95 V (see Fig. 1) and ~1.3 V (see our previous work [17]) at 180 °C (non-humidified). The reported low temperature cathode voltage cycling led to the formation of a metal band at the catalyst layer/membrane interface concomitant with a depletion of the Pt (metal) density in the vicinity to the interface towards the catalyst layer. The same effects have been observed in our study – Fig. 6b demonstrates the formation of the metal band at the membrane/catalyst layer interface. A comparison of Fig. 6a and b reveals a clear intensity change of the cathode catalyst layer for the SSS cycled cathode vs. the pristine cathode (note, the intensity of both anodes are identical), clearly indicating the metal depletion of the complete cathode catalyst layer upon SSS cycling. This difference of metal gradient formation in the low-temperature cathode vs. complete depletion in the intermediate-temperature cathode may be ascribed to the significantly higher potentials applied in the latter tests. However, by looking at the 5–7 μm thick metal band on the cathode in the SSS cycled intermediate temperature MEA, it is quite surprising, how 'well' the cathodes are still working despite all the degradation described. A quick estimation may help to understand this effect: assuming a dense Pt layer is formed from the 1 mg_{metal} cm^{-2} loaded cathodes, the resulting layer thickness may be in the range of approximately 0.5 μm. Therefore, it is very likely that the 5–7 μm formed metal layer is highly porous, basically resembling an in situ created nanostructured 'Pt-black' with all its advantages/disadvantages over supported Pt-based catalysts [45–49]. Therefore, kinetically the catalyst is assumed to still work properly and the observed kinetic overpotentials are assumed to be basically just an effect of the Pt surface area reduction. Detailed studies on this effect have not been performed here, but will be the topic of future work. As mentioned previously, the main effects, especially with the Vulcan supported catalysts, are seen in the mass transport regime which can clearly be correlated with oxidation of the carbon support to CO_2. For all three different cathodes, the catalyst layer thickness is reduced after SSS cycling. Especially for the Vulcan supported catalysts, the thickness is reduced by approximately 25–30% based on the initial thickness, whereas for the cathode with the corrosions stabilized carbon support the thickness reduction amounts only to ~10%. Significant thickness reductions during start–stop cycling has first been reported by Reiser et al. [19], but also other extreme transient operation conditions like local fuel starvation [50,51], extended operation at OCV [22] or voltage cycling up to carbon oxidation potentials [39] have been reported. All the thickness reduction referred in the literature is related to the corrosion of the carbon support of the catalysts and increased mass transport resistances are mainly caused typically under extreme conditions, before the integrity of the cathode itself is hampered. Especially in the case of fuel cells with liquid electrolytes, the mass transport overpotentials due to carbon corrosion are induced by the increased flooding of the cathode with electrolyte.

Some of the results and observations from this present study have been reported in the literature, specifically effects of start–stop operation were extensively studied in low temperature PEFCs and we could demonstrate that there are some commonalities between effects observed in intermediate and low temperature fuel cell operation, respectively. We finally would like to attempt a correlation of the findings from the simulated start–stop test with the cathode using the corrosion stabilized carbon support with a more realistic test; here we operated the MEA for 4000 h with a daily shutdown (total of 157 start/stops). Interestingly, just by simply comparing the kinetic and mass transport losses with respect to beginning of life, some surprising result can be found: both kinetic and mass transport overpotentials of the realistic durability test are almost identical with the simulated start–stop test, *viz.* 31 mV vs. 35 mV as increase of the ORR overpotentials at 0.1 A cm^{-2} for the 4000 h/157 stops test and the simulated start–stop test, respectively. Very similar effects can be observed for the increase of mass transport overpotentials at 0.7 A cm^{-2} with 23 mV for the 4000 h/157 stops test vs. 20 mV in the SSS test using the same cathode material. Additionally, the build-up of the metal layer at the catalyst/membrane interface can clearly be observed (Fig. 6c), although its thickness is only 1–2 μm, significantly thinner than the 5–7 μm as measured after the SSS test. The origin of the differing metal film thickness is not yet fully resolved; one might speculate that differences in the temperatures during the passing of the H_2/air fronts and the residence time might cause the different structure (see discussion below), another unknown parameter is the porosity of the two metal films which might differ for several reasons. In order to judge if these similar findings (increases of the overpotentials and formation of a dense metal layer at the membrane interface) are just coincidental or if a true correlation between the rapid aging in the SSS test and the 4000 h test can be drawn, the experimental conditions of the two tests need to be analyzed in detail. Both tests have been nominally operated at the identical temperature (180 °C) for approximately the same number of start–stop cycles (150 vs. 157 cycles), but we need to remember the drivers for the degradation during start–stop operation: (i) the presence and the residence time of a H_2/air (air/H_2) front in the fuel electrode flowfield; (ii) the temperature of the fuel cell when the H_2/air (air/H_2) front is passing through the fuel electrode flowfield and (iii) the transient potential reached the cathode during the passing of the H_2/air (air/H_2) front. As mentioned previously, the residence time in the SSS test is well defined (3 s), whereas in the case of the realistic test, it is pretty undefined. The same is

valid for the temperature during the passing of the H_2/air (air/H_2) front. In the case of the SSS test, the temperature is well defined (180 °C), whereas in the realistic test the situation is different. During the stop phase, the flows in both electrodes are stopped and air is allowed to diffuse into the fuel electrode flowfield during the slow cooling down of the fuel cell. That means, the residence time of the front is pretty long. In terms of OCV drop, it takes ca. 8 min to drop the OCV below 0.9 V and approximately 25 min to drop below 0.6 V. However, the temperature also drops to approximately 165 °C in the first 8 min and to 140 °C in the first 25 min after switching off the gases. During the start-up, the residence time is more defined, once the cell reaches a temperature of 80 °C, the anode side is purged with hydrogen at a flow of 3.3 NL h^{-1}, *i.e.*, the residence time in this case is also three seconds. Looking at this comparison, in the realistic test mainly the stop procedure appears to cause corrosive condition and leads to massive degradation since here long residence times at temperatures above 140 °C are present. In the start phase, the residence time is short and the front is only present at 80 °C, where degradation may also occur, however, the reaction kinetics are negligible compared to the stop phase. Although the residence time during the stop phase is pretty long leading to an almost standing H_2/air front, the decreasing temperature helps reducing degradation kinetics on the air electrode. Another point which may explain the similarity in kinetic overpotential increase in both tests and differing Pt-film thickness at EOL at the membrane/CL interface need to be mentioned. Considering acid evaporation rates at 180 °C of approximately 2 μg m^{-2} s (see e.g., Refs. [17,35]), roughly 8% of the initial MEA acid content have been evaporated at the end of the 4000 h/157 SS test, whereas the acid evaporation in the SSS test is negligible (total operation time of ca. 24 h). Since acid evaporation from the MEA cannot be located (*i.e.*, it is unknown if acid is evaporating from GDL, CL or membrane), it can at least not be ignored when kinetic comparison are made with the SSS MEA. Further experiments to detect acid content in catalyst layers in situ would be needed for clarification of this point. One method to be used in the future may be in situ X-ray imaging as demonstrated in Ref. [52] for intermediate temperature fuel cells. Nevertheless, the simulated start–stop procedure can be used as an accelerated aging tool, resulting in very similar effects than a realistic test covering 4000 h with identical numbers of start–stop cycles. These data are certainly promising for the development of rapid aging tools and their correlation to realistic durability tests, but they also demonstrate that there are still many lessons to be learned for complete lifetime predictions, especially if one considers that realistic tests are often far away from the well-defined laboratory environment.

6. Conclusion

In this paper, we studied the stability and degradation of several different cathode catalyst materials in simulated start–stop operation. The cathode catalysts consist of Pt/Vulcan XC72, Pt-alloy/Vulcan XC72 and Pt-alloy supported on a corrosion-stabilized carbon. The major findings on degradation during the simulated start–stop can be summarized: (i) kinetic losses for both alloy electrodes are almost identical and significantly lower than on the pure Pt-catalyst electrode; (ii) mass transport losses on the Vulcan XC72 supported catalysts are identical and significantly higher than mass transport losses on the electrodes using the stabilized carbon as catalyst support; (iii) as expected, no correlation between kinetic losses and relative amounts of oxidized carbon support is found but the increase of mass transport overpotentials is a clear function of amount of oxidized carbon from the catalyst support. Therefore, the combination of a Pt-alloy with a corrosion stabilized carbon support helps to manufacture very degradation resistant membrane electrode assemblies, especially under transient operation conditions like start–stop cycling. Finally, we made an attempt to correlate the findings from the simulated start–stop cycling with the most stable cathode material with data from a durability test over 4000 h and 157 start–stops, where almost identical changes in MEA properties have been found, which demonstrates the usefulness of our approach for lifetime predictions in future cathode developments.

Acknowledgements

We gratefully acknowledge experimental support from J. Weiser, M. Jantos and F. Rat.

Appendix A. Supplementary data

Supplementary data associated with this article can be found, in the online version, at doi:10.1016/j.jpowsour.2011.01.044.

References

[1] F.N. Büchi, M. Inaba, T.J. Schmidt, Polymer Electrolyte Fuel Cell Durability, Springer, NY, 2009.
[2] W. Vielstich, H. Yokokawa, H.A. Gasteiger, Handbook of Fuel Cells–Fundamentals, Technology and Applications, in: W. Vielstich, H. Yokokawa, H.A. Gasteiger (Eds.), Vol. 5 and 6, John Wiley and Sons, NY, 2009.
[3] P. Mocotéguy, B. Ludwig, J. Scholta, R. Barrera, S. Ginocchio, Fuel Cells 9 (2009) 325–348.
[4] V.P. McConnell, Fuel Cells Bull. 12 (2009) 12–16.
[5] P. Mocotéguy, B. Ludwig, J. Scholta, Y. Nedellec, D.J. Jones, J. Rozière, Fuel Cells 10 (2010) 299–311.
[6] T.J. Schmidt, J. Baurmeister, ECS Trans. 16 (2) (2008) 263–270.
[7] Q. Li, R. He, J.O. Jensen, N.J. Bjerrum, Fuel Cells 4 (2004) 147–159.
[8] T.J. Schmidt, J. Baurmeister, ECS Trans. 3 (1) (2006) 861–869.
[9] M. Yoshitake, A. Watakabe, Adv. Pol. Sci. 215 (2008) 127–155.
[10] B. Du, R. Pollard, J.F. Elter, M. Ramani, Performance and durability of a polymer electrolyte fuel cell operating with reformate: effects of CO, CO_2, and other trace impurities, in: F.N. Buechi, M. Inaba, T.J. Schmidt (Eds.), Polymer Electrolyte Fuel Cell Durability, Springer, NY, 2009, pp. 341–366.
[11] S.A. Gürsel, L. Gubler, B. Gupta, G.G. Scherer, Adv. Pol. Sci. 215 (2008) 157–217.
[12] T.J. Schmidt, K. Simbeck, G.G. Scherer, J. Electrochem. Soc. 152 (2005) A93–A97.
[13] D.N. Patel, H.C. Maru, M. Farooque, C.H. Ware, J. Electrochem. Soc. 131 (1984) 2750–2756.
[14] J. Antoni, Design of Experiments for Scientists and Engineers, Butterworth-Heinemann, London, 2003.
[15] P.J. Ross, Taguchi Techniques for Quality Engineering, McGraw-Hill, New-York, 1996.
[16] M. Hicks, D. Pierpoint, Application of accelerated testing and statistical lifetime modeling to membrane electrode assembly development, in: F.N. Buechi, M. Inaba, T.J. Schmidt (Eds.), Polymer Electrolyte Fuel Cell Durability, Springer, NY, 2009, pp. 385–396.
[17] T.J. Schmidt, High-temperature PEFCs: durability insights, in: F.N. Buechi, M. Inaba, T.J. Schmidt (Eds.), Polymer Electrolyte Fuel Cell Durability, Springer, NY, 2009, pp. 199–221.
[18] R. Makharia, S.S. Kocha, P.T. Yu, M.A. Sweikart, W. Gu, F.T. Wagner, H.A. Gasteiger, ECS Trans. 1 (8) (2006) 3–18.
[19] C.A. Reiser, L.J. Bregoli, T.W. Patterson, J.S. Yi, J.D. Yang, M.L. Perry, T.D. Jarvi, Electrochem. Solid State Lett. 8 (2005) A273.
[20] P.T. Yu, W. Gu, R. Makheria, F.T. Wagner, H.A. Gasteiger, ECS Trans. 3 (1) (2006) 797–809.
[21] W. Gu, R.N. Carter, P.T. Yu, H.A. Gasteiger, ECS Trans. 11 (1) (2007) 963–973.
[22] H. Chizawa, Y. Ogami, H. Naka, A. Matsunaga, N. Aoki, T. Aoki, K. Tanaka, ECS Trans. 11 (1) (2007) 981–992.
[23] K. Kinoshita, Carbon, in: Electrochemical and Physicochemical Properties, John Wiley & Sons, New York, 1988.
[24] N.M. Markovic, T.J. Schmidt, B.N. Grgur, H.A. Gasteiger, R.J. Behm, P.N. Ross, J. Phys. Chem. B 103 (1999) 8568–8577.
[25] M. Pourbaix, Atlas of Electrochemical Equilibria in Aqueous Solutions, National Association of Corrosion Engineers, Houston, Tx, USA, 1974.
[26] L. Tang, B. Han, K. Persson, C. Friesen, T. He, K. Sieradziki, G. Ceder, J. Am. Chem. Soc. 132 (2010) 596–600.
[27] M.L. Perry, T.W. Patterson, C.A. Reiser, ECS Trans. 3 (1) (2006) 783.
[28] M.L. Perry, R.M. Darling, S. Kandoi, T.W. Patterson, C.A. Reiser, Operating requirements for durable polymer-electrolyte fuel cell stacks, in: F.N. Buechi, M. Inaba, T.J. Schmidt (Eds.), Polymer Electrolyte Fuel Cell Durability, Springer, NY, 2009, pp. 399–417.
[29] T.J. Schmidt, ECS Trans. 1 (8) (2006) 19–31.
[30] J. Mader, L. Xiao, T.J. Schmidt, B.C. Benicewicz, Adv. Pol. Sci. 216 (2008) 63–124.
[31] S. Kocha, Principles of MEA preparation of PEM fuel cells, in Handbook of Fuel Cells–Fundamentals, Technology and Applications, in: W. Vielstich, H.A. Gasteiger, A. Lamm (Eds.), Vol. 3, John Wiley and Sons, NY, 2003, pp. 538–565.

[32] T.J. Schmidt, J. Baurmeister, J. Power Sources 176 (2008) 428–434.
[33] K.C. Neyerlin, H.A. Gasteiger, C.K. Mittelstaedt, J. Jorne, W. Gu, J. Electrochem. Soc. 152 (6) (2005) A1073–A1080.
[34] CRC Handbook of Chemistry and Physics, CRC Press, Boca Raton, FL, 2005.
[35] D.C. Steel, B.C. Benicewicz, L. Xiao, T.J. Schmidt, High-temperature polybenzimidazole membranes, in: W. Vielstich, H. Yokokawa, H.A. Gasteiger (Eds.), Handbook of Fuel Cells—Fundamentals, Technology and Applications, Vol. 5, John Wiley and Sons, NY, 2009, pp. 300–312.
[36] D.A. Landsman, F.J. Luczak, Catalyst studies and coating technologies, in hand book of fuel cells—fundamentals, In: W. Vielstich, H.A. Gasteiger, A. Lamm (Eds.), Handbook of Fuel Cells-Fundamentals, Technology and Applications, Vol. 2, John Wiley and Sons, Chichester, 2003, p. 811.
[37] U.A. Paulus, A. Wokaun, G.G. Scherer, T.J. Schmidt, V. Stamenkovic, N.M. Markovic, P.N. Ross, J. Phys. Chem. B 106 (2002) 4181–4191.
[38] V. Stamenkovic, T.J. Schmidt, N.M. Markovic, P.N. Ross, J. Phys. Chem. B 106 (2002) 11970–11979.
[39] S. Chen, H.A. Gasteiger, K. Hayakawa, T. Tada, Y. Shao-Horn, J. Electrochem. Soc. 157 (2010) A82–A97.
[40] S.C. Ball, S.L. Hudson, J.H. Leung, A.E. Russell, D. Thompsett, B.R.C. Theobald, ECS Trans. 11 (1) (2007) 1247–1257.
[41] P.J. Ferreira, G.J. la O', Y. Shao-Horn, D. Morgan, R. Makharia, S. Kocha, H.A. Gasteiger, J. Electrochem. Soc. 152 (2005) A2256–A2271.
[42] W. Bi, T.F. Fuller, ECS Trans. 11 (1) (2007) 1235–1246.
[43] M. Chatenet, E. Guilminot, C. Iojoiu, J.-Y. Sanchez, E. Rossinot, F. Maillard, ECS Trans. 11 (1) (2007) 1203–1214.
[44] P.N. Ross Jr., Deactivation and poisoning of fuel cell catalysts, in: E.E. Petersen, A.T. Bell (Eds.), Catalyst Deactivation, Marcel Dekker, Inc., New York, 1987, pp. 167–187, Chapter 7.
[45] M.K. Debe, A.K. Schmoekel, G.D. Vernstrom, R. Atanasoski, J. Power Sources 161 (2006) 1002–10011.
[46] G.C.K. Liu, R.J. Sanderson, G.D. Vernstrom, D.A. Stevens, R.T. Atanasoski, M.K. Debe, J.R. Dahn, J. Electrochem. Soc. 157 (2010) B207–B214.
[47] N. Ramaswamy, T.M. Arruda, W. Wen, N. Hakim, M. Saha, A. Gully, S. Mukerjee, Electrochim. Acta 54 (2009) 6756–6766.
[48] H.A. Gasteiger, S.S. Kocha, B. Sompalli, F.T. Wagner, Appl. Catal. B: Environ. 56 (2005) 9–35.
[49] H.A. Gasteiger, N.M. Markoivc, Science 324 (2009) 48–49.
[50] W. Patterson, R. Darling, Electrochem. Solid State Lett. 8 (2006) A183.
[51] R.N. Carter, W.B. Gu, B. Brady, P.T. Yu, K. Supramanian, H.A. Gasteiger, Handbook of Fuel Cells-Fundamentals, Technology and Applications, in: W. Vielstich, H.A. Gasteiger, H. Yokogawa (Eds.), Vol. 5, John Wiley & Sons, Chichester, 2009, 829.
[52] W. Maier, T. Arlt, C. Wannek, I. Manke, H. Riesemeier, P. Krüger, J. Scholta, W. Lehnert, J. Banhart, D. Stolten, Electrochem. Commun. 12 (2010) 1436–1438.